applied sciences

MDPI

Article

Wind Effects on Heating Demand and Threshold Exceedances in a Geodesic Habitat at Jezero Crater, Mars

Gonca Görmez [1] and Domenico Mazzeo [2,*]

[1] Department of Mechanical Engineering, Faculty of Engineering and Natural Sciences, Bursa Technical University, 16310 Bursa, Türkiye; gonca.gormez@btu.edu.tr

[2] Department of Energy, Politecnico di Milano, 20156 Milan, Italy

* Correspondence: domenico.mazzeo@polimi.it

Featured Application

The proposed TRNSYS–Python framework can support preliminary thermal design and heating-demand assessment of geodesic habitats for future Mars missions. By integrating facet-resolved solar irradiance calculations with transient thermal modeling and Martian climate data, the framework enables the evaluation of seasonal heating requirements and wind effects under Jezero Crater conditions.

Abstract

This study evaluates the heating demand of a geodesic Martian habitat at Jezero using meteorological inputs from the Mars Climate Database 6.1 and a coupled TRNSYS–Python thermal model. WIND and an idealized ZERO WIND reference, retaining the spherical conduction limit without explicitly modelling natural convection, were compared through annual and daily heating demand, environmental correlations, and threshold-exceedance indicators. Annual heating energy reached 336.78 MWh under WIND and 328.78 MWh under ZERO WIND, representing a 2.43% increase. Both scenarios exhibited their maximum daily demand on Sol 538, with 552.87 and 541.10 kWh, respectively. At a common daily energy threshold of 525.16 kWh/sol, exceedances occurred on 171 sols under WIND and 115 sols under ZERO WIND; the longest uninterrupted exceedance periods were 169 and 112 sols. WIND produced higher exceedance indicators across all tested thresholds. These findings suggest that a modest difference in annual heating energy can accompany a greater persistence of elevated daily demand. The indicators complement annual energy assessment by characterizing demand exceedances rather than heating-system failure.

Keywords: Martian habitat; geodesic dome; transient thermal modeling; facet-resolved solar irradiance; TRNSYS–Python simulation; Mars Climate Database (MCD); heating energy demand; Jezero Crater; wind effects

Academic Editor: Constantinos A. Balaras

Received: 19 October 2026
Revised: 17 November 2026
Accepted: 19 November 2026
Published: 20 November 2026

Copyright: © 2026 by the authors. Licensee MDPI, Basel, Switzerland. This article is an open access article distributed under the terms and conditions of the Creative Commons Attribution (CC BY) license.

1. Introduction

The thermal design of Martian habitats requires consideration of environmental conditions that differ substantially from those on Earth. Mars exhibits pronounced seasonal variations in its radiative energy balance, while atmospheric dust and solar geometry influence the distribution of surface irradiance [1,2]. Extreme temperature cycles also affect the thermal and mechanical behavior of potential habitat structures [3]. Numerical general circulation models have advanced the representation of Martian atmospheric

processes [4]. Multi-model assessments of Jezero Crater have nevertheless demonstrated variability in predicted atmospheric conditions, particularly in near-surface wind characteristics [5].

Observations from the Perseverance rover have substantially improved the characterization of Jezero's environment. The Mars Environmental Dynamics Analyzer (MEDA) provides measurements of atmospheric and surface conditions [6], revealing distinct daytime convective and nighttime stable regimes [7,8]. Measurements of the surface energy budget have further quantified solar and infrared radiative exchanges [9], while aerosol observations have identified diurnal and seasonal variations in atmospheric optical depth [10]. Together, these findings establish an observational basis for representing the thermal boundary conditions of a hypothetical Martian habitat.

Beyond temperature and radiation, Jezero exhibits variable atmospheric dynamics. Wind measurements have revealed recurring diurnal patterns, turbulence, and transient air-temperature fluctuations [11,12], while pressure observations have characterized atmospheric tides and disturbances [13]. Convective vortices and dust devils contribute to local dust activity and produce observable radiative effects [14,15]. Changes in surface albedo and dust accumulation have also been documented [16,17], including observations during a regional dust storm [18]. Such environmental variability provides the basis for examining habitat thermal performance under time-dependent climatic conditions.

Previous studies have examined Martian habitat thermal performance at different levels of modelling detail. Jadeja et al. [19] combined PlanetWRF environmental simulations with Ecotect and computational fluid dynamics to investigate the orientation, envelope properties, and thermal comfort of a rectangular habitat. Salgado-Rodriguez et al. [20] investigated a conceptual Martian base through theoretical thermal analysis, an ESATAN case study, and parameter sensitivity analysis. Kömle et al. [21] addressed site selection and solar irradiation and heat-transfer modelling for an inflatable habitat in Valles Marineris. Görmez [22] used an MCD-driven lumped TRNSYS model to assess heating-demand exceedances, while excluding solar and internal heat gains. Their findings emphasize different aspects of habitat performance. Charoenboonvivat and de Weck [23] developed an hourly thermal power demand model within HabNet and examined a hemispherical Martian habitat over a 24-h period, considering variations in envelope properties and heat-transfer parameters. Salgado-Rodriguez et al. [20] highlighted the importance of thermal insulation between the module and the Martian ground, whereas Kömle et al. [21] identified locations within Valles Marineris with sufficient solar illumination to support greenhouse and photovoltaic operation. Görmez [22] reported site-dependent heating-demand patterns and showed that average energy indicators alone do not adequately describe the persistence of elevated demand. These findings motivate consideration of both heat-transfer processes and the temporal distribution of heating requirements, without implying direct quantitative comparability between different habitat designs. The present study combines facet-resolved solar gains with transient thermal modelling to compare wind-dependent heating demand and the persistence of elevated daily demand at Jezero.

Separately, geodesic dome studies have examined solar transmission through individual triangular panels [24] and the thermal and electrical performance of triangular photovoltaic modules [25]. These studies provide a basis for facet-dependent solar modelling.

The present study uses a coupled TRNSYS–Python framework integrating facet-resolved solar irradiance calculations with three-node transient thermal modeling. A geodesic habitat comprising 656 triangular facets is represented in the solar calculations,

while its thermal response is described by the envelope, indoor air, and floor. Using MCD 6.1 climate data, heating requirements are evaluated over approximately one Martian year under scenarios with and without wind. The principal methodological contribution lies in combining solar irradiance calculations for 656 individually oriented triangular facets with a three-node transient thermal model, enabling the assessment of annual heating demand and the frequency, persistence, and severity of elevated daily demand under matched Martian climate conditions with and without imposed wind.

2. Materials and Methods

This section describes the environmental inputs, habitat geometry, heat-transfer formulation, and numerical procedures used in the simulations. Figure 1 summarizes the modelling framework.

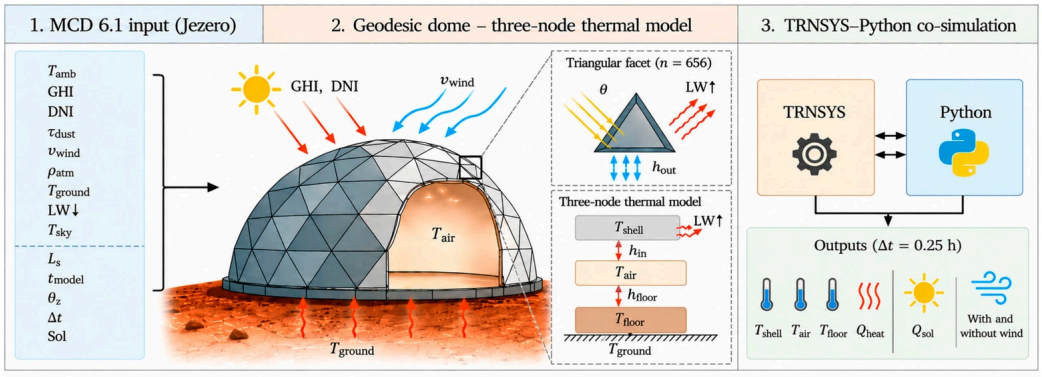

Figure 1. Schematic representation of the TRNSYS 18–Python 3.10.11 modeling framework, integrating Martian climate data, facet-resolved solar irradiance calculations, and three-node transient thermal analysis.

2.1. Study Area and Martian Climate Data

Jezero Crater (18.4° N, 77.5° E) was selected as the location of the hypothetical habitat. Meteorological boundary conditions were obtained from the Mars Climate Database (MCD), version 6.1. The MCD provides atmospheric and surface fields derived from numerical climate simulations and associated postprocessing. These fields represent modelled environmental conditions rather than a continuous record of in situ weather observations [4,26]. Variable definitions and extraction options were interpreted using the MCD 6.1 User Manual [27].

The meteorological dataset provides hourly atmospheric pressure, atmospheric density, air and ground temperatures, horizontal wind components, solar zenith angle, dust optical depth, shortwave radiation, and downward longwave radiation. Surface variables were extracted separately, while atmospheric variables were sampled at a reference height of 9.1416 m above the local surface. This height corresponds to the nominal habitat diameter and defines the adopted atmospheric sampling level; it does not represent the dome apex height. The available extraction script is configured for the cold scenario (scenario 8), with low atmospheric dust loading, minimum solar extreme-ultraviolet forcing, high-resolution mode, and no additional perturbations. The reference height is measured above the local surface and should not be interpreted as terrain elevation relative to the Martian areoid [27]. A numerical areoid-referenced terrain elevation was not recorded in the exported dataset. The adopted forcing represents a location-specific cold-scenario case rather than the range of conditions across Jezero Crater. Its representativeness for other potential deployment sites within the crater has not been assessed.

The underlying MCD atmospheric fields are stored on a 5.625° longitude × 3.75° lat-

itude grid. The high-resolution mode uses MOLA topography at 32 pixels/degree to refine surface pressure and reconstruct atmospheric profiles [27,28]. In this study, meteorological variables were extracted at one-Earth-hour intervals at the selected coordinates; this sampling interval does not imply an equivalent native meteorological resolution. Surface fields and atmospheric conditions at the prescribed reference height provide the environmental forcing for the thermal model, but do not resolve habitat-induced flow disturbances or local gusts. Their site-specific near-surface accuracy was not independently evaluated.

Seasonal progression was represented by calculating solar longitude using a simplified Keplerian orbital model, following the orbital framework described by Allison and McEwen [29].

2.2. Habitat Geometry and Material Properties

The habitat was represented as a hemispherical enclosure with a nominal internal volume of 200 m^3. The nominal radius was calculated from the hemispherical volume as

$$r = \left(\frac{3V}{2\pi}\right)^{1/3}, \quad (1)$$

where r is the nominal radius (m) and V is the prescribed internal volume (m^3). The resulting radius and diameter were 4.5708 m and 9.1416 m, respectively, with a circular floor area of 65.6343 m^2. These dimensions define the idealized geometry adopted in the present model.

The envelope geometry was generated through three successive subdivisions of an icosahedron, followed by projection onto a spherical surface and clipping at the equatorial plane. The resulting mesh comprised 656 triangular facets with a combined surface area of 130.6431 m^2. These dimensions were calculated from the implemented geometry; the nominal volume refers to the analytical hemisphere.

Facet areas and outward normal vectors were used to determine the distribution of incident solar radiation. The thermal response was represented by three coupled nodes corresponding to the shell, indoor air, and floor. Each facet therefore contributed separately to the solar-gain calculation, while the shell was assigned a single temperature. The floor was represented as an equivalent thermal mass without resolving individual construction layers.

Facet orientation determines direct-beam incidence and the sky-view weighting of isotropic diffuse irradiance; the resulting contributions are summed using facet areas. In contrast, external convection is represented by a common heat-transfer coefficient evaluated from wind speed, atmospheric properties, and the shell temperature. Wind direction and differences between windward and leeward facets are not resolved. The model therefore accounts for orientation-dependent solar gains but not spatial variations in shell temperature or local convective heat flux. The influence of these geometric and thermal simplifications on predicted heating demand has not been quantified.

An equivalent shell thickness of 18 mm was selected with reference to the preliminary membrane-thickness estimate reported by Salgado-Rodriguez et al. [20] for a conceptual Martian dome. Their estimate was based on initial structural calculations considering the pressure difference across the membrane. In the present study, this thickness was used to calculate the shell mass and lumped thermal capacitance. Its structural suitability for the proposed geodesic geometry was not evaluated.

The density and specific heat capacity were prescribed as 1700 kg/m^3 and 1172 J/(kg·K), respectively, using the typical ETFE properties reported by Chemours [30].

These reference values were held constant; their temperature dependence under the simulated Martian conditions was not represented.

The shell thermal capacitance was calculated as

$$C_{\text{shell}} = \rho_{\text{shell}} c_{p,\text{shell}} \delta_{\text{shell}} A_{\text{shell}} \quad (2)$$

where C_{shell} is the shell thermal capacitance (J/K), ρ_{shell} is the shell density (kg/m^3), $c_{p,\text{shell}}$ is the specific heat capacity (J/(kg·K)), δ_{shell} is the shell thickness (m), and A_{shell} is the total area of the triangular facets (m^2). The adopted parameters yield a shell thermal capacitance of 4.6853 MJ/K. Through-thickness temperature gradients were not resolved in the single-node shell representation. Accordingly, no explicit shell-conduction resistance or separate insulation layer was included, and an ETFE thermal-conductivity value was not used in the governing equations. The equivalent thickness determines shell thermal capacitance rather than insulation performance. The adopted envelope therefore represents a conceptual thermal configuration, not a qualified construction specification for a pressurized Martian habitat.

Solar absorptance, longwave emissivity, and longwave transmittance were prescribed as 0.10, 0.89, and 0.11, respectively, adopting the ETFE inputs listed in Table 7 of Salgado-Rodriguez et al. [20]. The shortwave solar transmittance was prescribed as 0.90, based on the reference value reported by Chemours for a 0.050 mm ETFE film [30]. The application of this value to the adopted 18 mm equivalent shell represents a modelling assumption and does not imply that the same transmittance has been experimentally demonstrated for the specified thickness. All optical coefficients were maintained constant throughout the simulations.

The indoor-air density and specific heat capacity were prescribed as 1.20 kg/m^3 and 1007 J/(kg·K), respectively. The corresponding thermal capacitance was calculated as

$$C_{\text{air}} = \rho_{\text{air}} \, c_{p,\text{air}} \, V, \quad (3)$$

where C_{air} is the indoor-air thermal capacitance (J/K), ρ_{air} is the indoor-air density (kg/m^3), $c_{p,\text{air}}$ is the indoor-air specific heat capacity (J/(kg·K)), and V is the nominal internal volume (m^3). These inputs yielded an indoor-air thermal capacitance of 0.24168 MJ/K. The floor thermal capacitance was prescribed as 5.0 MJ/K. The indoor-air properties and floor capacitance were fixed model inputs rather than parameters calibrated against habitat measurements.

The shell-to-air, floor-to-air, and floor-to-ground heat-transfer coefficients were each prescribed as 3.0 W/(m^2·K). The numerical value of the ground-coupling coefficient is also used by Salgado-Rodriguez et al. [20], although their module-to-ground configuration differs from the floor-to-ground representation adopted here. The longwave emissivities of the floor and surrounding ground were set to 0.90 and 0.95, respectively, as model assumptions.

2.3. Facet-Resolved Solar Irradiance and Heat Gains

Solar irradiance was evaluated separately for the 656 triangular facets using their areas and outward unit normal vectors. The meteorological inputs comprised global horizontal irradiance, direct horizontal irradiance, direct normal irradiance, solar zenith angle, solar longitude, and model local solar time. Diffuse horizontal irradiance was obtained as

$$G_{\mathrm{dh}} = \max\left(0, G_{\mathrm{h}} - G_{\mathrm{bh}}\right), \tag{4}$$

where G_{dh} is diffuse horizontal irradiance, G_{h} is global horizontal irradiance, and G_{bh} is direct horizontal irradiance, all expressed in W/m^2.

The solar direction was constructed using the supplied solar zenith angle and an azimuthal direction calculated from the site latitude, solar longitude, and model local solar time. Solar declination and hour angle were calculated as

$$\delta = \arcsin\left(\sin\varepsilon \sin L_s\right), \tag{5}$$

$$H = 15^\circ \left(\frac{t_{\mathrm{loc}}}{1\ \mathrm{h}} - 12\right) \tag{6}$$

where δ is solar declination, $\varepsilon = 25.19^\circ$ is the adopted Martian obliquity, L_s is solar longitude, H is the hour angle, and t_{loc} is the model local solar time on a 24-h scale. The relationship between declination, obliquity, and solar longitude follows the Mars solar geometry described by Allison and McEwen [29] and the NASA Mars24 technical notes [31]. The local-hour coordinate was calculated from the fractional sol and supplied to the MCD local true solar time input [26], without an equation-of-time correction.

In the local east–north–up coordinate system, the horizontal directional components were calculated as

$$u_E = -\cos\delta \sin H, \qquad u_N = \cos\phi \sin\delta - \sin\phi \cos\delta \cos H, \tag{7}$$

where $\phi = 18.4^\circ$ is the site latitude, and u_E and u_N are dimensionless eastward and northward components. The solar unit vector was then formed as

$$\mathbf{s} = \left(\sin\theta_z \frac{u_E}{q}, \sin\theta_z \frac{u_N}{q}, \cos\theta_z\right), \qquad q = \sqrt{u_E^2 + u_N^2}, \tag{8}$$

where θ_z is the supplied solar zenith angle and q normalizes the horizontal direction. This implementation retains the meteorological zenith angle while deriving the horizontal solar direction from the model's seasonal and local-hour coordinates.

Direct irradiance on facet i was calculated using the cosine projection:

$$G_{\mathrm{b},i} = G_{\mathrm{bn}} \max\left(0, \mathbf{n}_i \cdot \mathbf{s}\right), \tag{9}$$

where $G_{\mathrm{b},i}$ is the direct irradiance on the facet (W/m^2), G_{bn} is direct normal irradiance (W/m^2), and $\mathbf{n}_i$ is the outward unit normal vector of the facet. The dot product represents the cosine of the incidence angle. This formulation follows the standard geometric projection of direct normal irradiance onto an inclined surface. Direct irradiance was set to zero when the solar zenith angle was at least 90° [32].

Diffuse irradiance was distributed using an isotropic sky approximation:

$$G_{\mathrm{d},i} = G_{\mathrm{dh}} \frac{1 + \cos\beta_i}{2}, \tag{10}$$

where $G_{\mathrm{d},i}$ is diffuse irradiance on facet i (W/m^2), and β_i is the facet inclination relative to the horizontal plane. In the implemented geometry, $\cos\beta_i$ equals the vertical component of $\mathbf{n}_i$. The factor $(1 + \cos\beta_i)/2$ represents the unobstructed sky-view factor used by the iso-

tropic model. This approximation assumes a uniform diffuse sky distribution [33].

The total solar power incident on the envelope was calculated by summing the facet contributions:

$$Q_{\mathrm{inc}} = \sum_{i=1}^{N} A_i \left(G_{\mathrm{b},i} + G_{\mathrm{d},i} \right), \tag{11}$$

where Q_{inc} is incident solar power (W), A_i is the area of facet i (m^2), and $N = 656$ is the number of facets. Ground-reflected shortwave radiation was not included in this calculation.

The absorbed and transmitted solar powers were determined as

$$Q_{\mathrm{abs}} = \alpha_{\mathrm{sol}} Q_{\mathrm{inc}}, \qquad Q_{\mathrm{trans}} = \tau_{\mathrm{sol}} Q_{\mathrm{inc}}, \tag{12}$$

where Q_{abs} and Q_{trans} are the absorbed and transmitted powers (W), and $\alpha_{\mathrm{sol}} = 0.10$ and $\tau_{\mathrm{sol}} = 0.90$ are the dimensionless optical coefficients specified in Section 2.2. The absorbed power was applied to the shell energy balance, while the transmitted power was assigned entirely to the floor node. This allocation is a lumped model assumption; the spatial distribution of transmitted radiation within the habitat was not resolved.

Global and direct horizontal irradiance were obtained from MCD 6.1, while direct normal irradiance was derived using the supplied solar zenith angle. Atmospheric attenuation is represented through the MCD surface irradiance inputs for the selected atmospheric scenario; no additional dust-dependent attenuation factor is applied in the habitat model. Facets facing away from the Sun receive no direct-beam contribution. However, this orientation-based treatment does not include a separate obstruction or shadow-casting calculation for structural members, nearby objects, or terrain. The diffuse component assumes an unobstructed isotropic sky. Dust deposition on the envelope and associated changes in its optical properties are not modelled.

2.4. Transient Thermal Model and Energy Balances

The transient thermal response was represented by three coupled nodes corresponding to the shell, indoor air and floor/effective thermal mass. This formulation retains separate energy-storage terms and heat exchanges between these components for the assessment of annual heating demand. Each node was assigned a uniform temperature and the thermal capacity specified in Section 2.2. Solar gains were calculated for individual facets and then aggregated into the shell and floor energy balances. Local temperature distributions and through-thickness shell gradients were not explicitly resolved. The governing equations were

$$C_s \frac{dT_s}{dt} = Q_{\mathrm{abs}} + h_o A_s \left(T_\infty - T_s \right) + h_{sa} A_s \left(T_a - T_s \right) + Q_{\mathrm{LW},s}, \tag{13}$$

$$C_a \frac{dT_a}{dt} = h_{sa} A_s \left(T_s - T_a \right) + h_{fa} A_f \left(T_f - T_a \right) + Q_{\mathrm{heat}}, \tag{14}$$

$$C_f \frac{dT_f}{dt} = Q_{\mathrm{trans}} + h_{fa} A_f \left(T_a - T_f \right) + h_g A_f \left(T_g - T_f \right) + Q_{\mathrm{LW},f}. \tag{15}$$

Here, T_s, T_a, and T_f denote the shell, indoor-air, and floor temperatures (K), respectively; T_∞ and T_g are the prescribed ambient-air and ground temperatures (K). The quantities C_s, C_a, and C_f are the node thermal capacities (J/K), A_s and A_f are the shell and floor

areas (m^2), and t is time (s). The coefficients h_o, h_{sa}, and h_{fa} describe external convection, shell–air exchange, and floor–air exchange, respectively, while h_g represents effective floor–ground thermal coupling; all have units of W/(m^2·K). The external coefficient is evaluated as described in Section 2.5.

The quantities Q_{abs} and Q_{trans} are the solar heat rates absorbed by the shell and transmitted to the floor node, respectively (W). Heating power, Q_{heat} (W), is supplied to the indoor-air node. The terms $Q_{LW,s}$ and $Q_{LW,f}$ denote net longwave radiative heat gains (W). Internal shell–air and floor–air exchanges appear with opposite signs in the connected node balances.

Longwave exchange was represented by a diffuse-grey radiation network with a semitransparent shell and an opaque floor. The formulation uses irradiation, radiosity, and view-factor relations; the underlying radiation concepts are described by Frei [34,35] The following expressions specify their implementation in the present model. Atmospheric longwave forcing is represented by an effective sky temperature derived from the MCD downward longwave flux; it is a radiative-equivalent temperature rather than the ambient-air temperature. The surrounding ground is treated as opaque, with a prescribed emissivity of 0.95, and its radiosity includes thermal emission at the supplied ground temperature and reflected atmospheric longwave radiation. Sky and ground contributions are combined using area-weighted facet view factors. The shell has prescribed longwave emissivity and transmittance values of 0.89 and 0.11, respectively, while the opaque interior floor has an emissivity of 0.90. The radiation network accounts for exchange on both sides of the shell and transmission of external longwave radiation into the enclosure. These properties are held constant, and the external radiative boundaries represent an unobstructed sky and horizontal surrounding ground.

For each exterior facet, the sky view factor was calculated from its orientation and then averaged over the shell area:

$$F_{\mathrm{sky},i} = \frac{1 + n_{z,i}}{2}, \qquad F_{\mathrm{sky}} = \frac{\sum_{i=1}^{N} A_i F_{\mathrm{sky},i}}{A_s}, \qquad F_{\mathrm{ground}} = 1 - F_{\mathrm{sky}}. \tag{16}$$

Here, A_i is the area of facet i (m^2), $n_{z,i}$ is the vertical component of its outward unit normal, and N is the number of facets. All view factors are dimensionless. This treatment represents an unobstructed sky and horizontal surrounding ground, with the area-weighted factors applied to the single shell temperature node.

The sky irradiation and surrounding-ground radiosity were calculated as

$$H_{\mathrm{sky}} = \sigma T_{\mathrm{sky}}^4, \tag{17}$$

$$J_g = \varepsilon_g \sigma T_g^4 + \left(1 - \varepsilon_g\right) H_{\mathrm{sky}}, \tag{18}$$

and the effective irradiation incident on the shell exterior was

$$H_{\mathrm{ext}} = F_{\mathrm{sky}} H_{\mathrm{sky}} + F_{\mathrm{ground}} J_g. \tag{19}$$

Here, T_{sky} is the prescribed effective sky temperature (K), ε_g = 0.95 is the adopted surrounding-ground emissivity, and σ = 5.670374419 × 10^{-8} W/(m^2·K^4) is the Stefan–Boltzmann constant. The quantities H_{sky}, J_g, and H_{ext} have units of W/m^2. Ground radiosity includes thermal emission and reflected sky irradiation. The surrounding ground acts as a prescribed radiative boundary rather than an additional thermal state.

Within the enclosure, the floor was assumed to view the shell completely. Area reciprocity and enclosure closure therefore give

$$F_{f\to s}=1, \qquad F_{s\to f}=\frac{A_f}{A_s}, \qquad F_{s\to s}=1-F_{s\to f}. \tag{20}$$

The notation $F_{i\to j}$ denotes the fraction of radiation leaving surface i that reaches surface j. The shell self-view factor accounts for its concave interior. These relations follow the standard view-factor framework [34].

With the adopted shell emissivity ε_s = 0.89 and longwave transmittance τ_{IR} = 0.11, the shell longwave reflectance is zero. The inward shell radiosity and floor radiosity consequently become

$$J_s=\varepsilon_s\sigma T_s^4+\tau_{IR}H_{ext}, \tag{21}$$

$$J_f=\varepsilon_f\sigma T_f^4+\left(1-\varepsilon_f\right)H_f, \qquad H_f=J_s, \tag{22}$$

while irradiation on the inner shell is

$$H_s=F_{s\to f}J_f+F_{s\to s}J_s. \tag{23}$$

Here, ε_f = 0.90 is the adopted floor emissivity. The quantities J_s and J_f are outgoing radiative fluxes, whereas H_s and H_f are incident radiative fluxes; all are expressed in W/m^2. The term $\tau_{IR}H_{ext}$ accounts for external longwave radiation transmitted through the shell into the enclosure.

The net longwave heat gains entering the thermal balances were

$$Q_{LW,s}=A_s\varepsilon_s\left(H_s+H_{ext}-2\sigma T_s^4\right), \tag{24}$$

$$Q_{LW,f}=A_f\left(H_f-J_f\right). \tag{25}$$

The shell expression includes absorption and emission at both its inner and outer surfaces. The floor expression represents its net radiative exchange with the enclosure. Positive values indicate heat gain by the corresponding node.

2.5. External Convective Heat Transfer

External convective heat transfer was represented using the sphere correlation proposed by Whitaker (1972) [36]. The nominal habitat diameter, D = 9.1416 m, was adopted as the characteristic length. Applying this sphere correlation to the ground-mounted dome constitutes a geometric approximation. Soria-Salinas et al. [37] experimentally evaluated convective heat-transfer correlations for sensor rods in low-pressure CO_2 flows. Domínguez-Pumar et al. [38] combined experiments and numerical modelling to investigate heat transfer around a miniature spherical wind sensor for Mars. The Whitaker correlation is used here as an engineering approximation; its applicability to the specific dome geometry and Martian conditions remains to be independently assessed. Accordingly, the predicted convection coefficients are treated as model estimates rather than experimentally validated values. The external convective heat-transfer coefficient was calculated as

$$h_o = \frac{Nu_D\, k_\infty}{D}, \tag{26}$$

where h_o is the external convective heat-transfer coefficient (W/(m^2·K)), Nu_D is the dimensionless Nusselt number, k_∞ is the CO_2 thermal conductivity evaluated at the ambient temperature (W/(m·K)), and D is the nominal diameter (m).

The documented applicability range of the Whitaker correlation does not encompass all simulated Reynolds numbers and viscosity ratios [39]. Sensitivity to this modelling choice was assessed through an annual WIND comparison with the Yuge formulation using film-temperature properties, while retaining the remaining model settings. The results and their limitations are discussed in Section 4.

For nonzero wind speed, the Nusselt number was evaluated using

$$Nu_D = 2 + \left(0.4Re_D^{1/2} + 0.06Re_D^{2/3}\right) Pr^{0.4} \left(\frac{\mu_\infty}{\mu_s}\right)^{1/4}. \tag{27}$$

Here, Re_D and Pr are the Reynolds and Prandtl numbers, respectively, while μ_∞ and μ_s are the CO_2 dynamic viscosities evaluated at the ambient and shell temperatures (kg/(m·s)). The Prandtl number was prescribed as Pr = 0.80 in the present implementation. The correlation accounts for the temperature dependence of viscosity through the ratio μ_∞/μ_s.

The Reynolds number was calculated as

$$Re_D = \frac{\rho_\infty U_\infty D}{\mu_\infty}, \tag{28}$$

where ρ_∞ is the atmospheric density (kg/m^3), and U_∞ is the wind speed (m/s). Atmospheric density, wind speed, and ambient temperature were supplied by the prepared meteorological inputs at the reference height specified in Section 2.1.

The temperature-dependent dynamic viscosity was evaluated using Sutherland's law [40]:

$$\mu(T) = \mu_{\mathrm{ref}} \left(\frac{T}{T_{\mathrm{ref}}}\right)^{3/2} \frac{T_{\mathrm{ref}} + S}{T + S}, \tag{29}$$

where $\mu(T)$ is dynamic viscosity (kg/(m·s)), T is temperature (K), μ_{ref} is the reference viscosity, T_{ref} is the reference temperature (K), and S is the Sutherland constant (K). This functional form follows the standard Sutherland viscosity model. The adopted constants were μ_{ref} = 0.0000147 kg/(m·s), T_{ref} = 293 K, and S = 240 K, consistent with the CO_2 viscosity formulation reported by Yamashita et al. [41].

The CO_2 thermal conductivity was calculated using the polynomial coefficients reported by Osczevski [42]:

$$k_\infty = aT_\infty^2 + bT_\infty + c, \tag{30}$$

where T_∞ is the ambient temperature (K), a = 0.00000011691 W/(m·K^3), b = 0.000013327 W/(m·K^2), and c = 0.0022469 W/(m·K). The source correlation uses the mean film temperature, whereas the Whitaker reference implementation evaluates it at the ambient-air temperature, T_∞, as a modelling approximation.

The resulting convective heat-transfer rate was

$$Q_{\mathrm{conv},o} = h_o A_s (T_\infty - T_s), \tag{31}$$

where $Q_{\mathrm{conv},o}$ is the external convective heat-transfer rate (W), A_s is the shell area (m^2), and T_s is the shell temperature (K). A positive value denotes heat gain by the shell. A single external coefficient was applied over the entire shell area. For the annual Yuge sensitivity comparison, the piecewise forced-convection correlation reproduced by Will et al. [39] was implemented:

$$Nu_Y = \begin{cases} 2 + 0.493 Re_{\mathrm{film}}^{0.50}, & 10 < Re_{\mathrm{film}} < 1800, \end{cases} \tag{32}$$

$$2 + 0.300 Re_{\mathrm{film}}^{0.57}, \; 1800 \le Re_{\mathrm{film}} < 150,000. \tag{33}$$

The film temperature was defined as the arithmetic mean of the shell and ambient-air temperatures:

$$T_{\mathrm{film}} = \frac{T_s + T_\infty}{2}. \tag{34}$$

The CO_2 viscosity and thermal conductivity were evaluated at this temperature using the functions specified above. Density was adjusted assuming unchanged pressure:

$$\rho_{\mathrm{film}} = \rho_\infty \frac{T_\infty}{T_{\mathrm{film}}}. \tag{35}$$

The Reynolds number and external convective heat-transfer coefficient were then calculated as

$$Re_{\mathrm{film}} = \frac{\rho_{\mathrm{film}} U_\infty D}{\mu(T_{\mathrm{film}})}, \qquad h_{o,Y} = \frac{Nu_Y \; k(T_{\mathrm{film}})}{D}. \tag{36}$$

For the ZERO WIND case, $U_\infty = 0$, and the implementation sets $Re_D = 0$ and $Nu_D = 2$, giving

$$h_{o,0} = \frac{2k_\infty}{D}. \tag{37}$$

Thus, setting wind speed to zero removes the wind-dependent contribution while retaining a nonzero baseline heat-transfer coefficient. This treatment does not constitute a separate natural-convection model.

2.6. Numerical Solution and Heating Control

TRNSYS supplies the meteorological inputs and heating setpoint to the Python 3.10.11 thermal model through Type3157. Python integrates the three-node energy balances over the time step supplied by TRNSYS and returns the node temperatures, solar gains, and step-average heating power. Repeated calls within the same time step are evaluated from the same previously committed thermal state; the updated state is committed only at the end of the time step, preventing repeated advancement during TRNSYS iterations. The supplied environmental inputs are held constant during each internal integration. This treatment and the finite heater-control iterations introduce numerical approximations. The checks reported in Section Numerical Consistency and Time-Step Sensitivity assess numerical consistency and short-period time-step

sensitivity.

The coupled energy balances were solved in Python through the TRNSYS [43] interface. The temperature state vector was defined as

$$\mathbf{T} = \begin{bmatrix} T_s & T_a & T_f \end{bmatrix}^{\mathsf{T}}, \qquad \frac{d\mathbf{T}}{dt} = \mathbf{f}\left(\mathbf{T}, \mathbf{u}, Q_{\text{heat}}\right), \tag{38}$$

where T_s, T_a, and T_f are the shell, indoor-air, and floor temperatures (K), respectively; t is time (s); $\mathbf{u}$ contains the meteorological boundary conditions and solar gains; and Q_{heat} is the heating power (W). The components of $\mathbf{f}$ represent the temperature rates obtained from the energy balances and have units of K/s.

The coupled energy balances were integrated using the classical fourth-order Runge–Kutta method [44], with eight internal substeps per 0.25 h TRNSYS interval. Meteorological inputs and trial heating power were held constant within each interval.

Heating was represented by an ideal, continuously adjustable thermal input to the indoor-air node, bounded by

$$0 \le Q_{\text{heat}} \le Q_{\max}, \qquad Q_{\max} = 100{,}000\ \text{W}. \tag{39}$$

The indoor-air setpoint was 22 °C (295.15 K). At each time step, the model first predicted the end-of-step temperature without heating. If this temperature reached or exceeded the setpoint, heating power was set to zero. Otherwise, a second prediction was performed at $Q_{\max}$. If the maximum power was insufficient to reach the setpoint, the maximum-power solution was retained.

For intermediate heating requirements, the controller sought a zero of

$$R(Q) = T_{a,n+1}(Q) - T_{\text{set}}, \tag{40}$$

where $R(Q)$ is the temperature residual (K), $T_{a,n+1}(Q)$ is the predicted indoor-air temperature at the end of time step n for a constant trial power Q (W), and T_{set} is the setpoint temperature (K).

Trial power was updated by bracketed linear interpolation, consistent with the false-position principle:

$$Q_c = Q_L + \frac{T_{\text{set}} - T_L}{T_U - T_L}\left(Q_U - Q_L\right), \tag{41}$$

where Q_L and Q_U are the lower and upper trial-power bounds (W), T_L and T_U are their predicted end-of-step air temperatures (K), and Q_c is the new trial power (W). The corresponding bound was updated after each prediction, and seven false-position iterations were performed [45]. Each trial started from the same previously committed temperature state.

No active cooling was modelled, and heating demand was reported as delivered thermal energy rather than electrical consumption. The initial temperatures of the shell, indoor air, and floor were set equal to the initial ground temperature.

Numerical Consistency and Time-Step Sensitivity

Numerical energy accounting was checked in separate short-duration runs by comparing each node's stored-energy change with its integrated net heat input, using the same Runge–Kutta quadrature. Internal exchanges cancelled in the overall balance, and the maximum absolute whole-system residual per integration interval was below

0.000002 J. This check establishes numerical consistency within the tested windows, rather than physical validation or time-step convergence.

Time-step sensitivity was examined for Sol 538 using matched initial thermal states and meteorological forcing at external time steps of 0.25 h and 0.125 h. The comparison assessed the combined effect of integration and heater-control time resolution.

These checks assess numerical consistency and local time-resolution sensitivity, rather than predictive accuracy against observations. No direct validation against habitat measurements or an independent reference model was performed. The critical-sol test does not establish annual time-step independence or the sensitivity of annual exceedance indicators.

2.7. Simulation Scenarios and Performance Indicators

Two simulation cases were considered to evaluate the influence of wind on habitat heating demand. In the WIND case, the meteorological wind-speed series was applied to the external convection model. In the ZERO WIND case, wind speed was set to zero while the remaining meteorological inputs, geometry, material properties, and heating-control settings were unchanged. In the ZERO WIND case, the adopted correlation reduces to Nu = 2, retaining the spherical conduction-limit contribution to external heat transfer. ZERO WIND is therefore an idealized zero-imposed-wind reference, not a representation of a physical calm atmosphere with buoyancy-driven natural convection. Radiation and the remaining thermal-model terms are retained, although their calculated heat rates may change with the resulting node temperatures. Thus, the comparison isolates the wind-dependent contribution within the adopted formulation rather than representing a complete forced-versus-natural convection comparison.

Performance was evaluated over approximately one Martian year after excluding the initial spin-up period. Complete sols were used for daily comparisons and demand-exceedance indicators, whereas the final partial sol was retained in the annual and seasonal energy assessments and correlation analysis.

Heating energy over an evaluation interval $\mathscr{B}$ was calculated as

$$E_{\mathscr{B}} = \frac{1}{1000} \sum_{k} Q_{\mathrm{heat},k} \ \Delta t_{k,\mathscr{B}}, \tag{42}$$

where $E_{\mathscr{B}}$ is heating energy (kWh), $Q_{\mathrm{heat},k}$ is the heating power assigned to simulation interval k (W), and $\Delta t_{k,\mathscr{B}}$ is the duration of its overlap with the evaluation interval (h). The factor 1/1000 converts Wh to kWh. Power was treated as constant within each 0.25 h simulation interval. Intervals crossing a sol boundary were divided according to their overlap durations, preserving total energy during aggregation.

Seasonal performance was evaluated over twelve solar-longitude intervals of 30°. Simulation intervals were assigned according to their associated meteorological solar longitude. Mean heating power was calculated as

$$\bar{P}_{\mathscr{B}} = \frac{E_{\mathscr{B}}}{\Delta t_{\mathscr{B}}}, \tag{43}$$

where $\bar{P}_{\mathscr{B}}$ is mean heating power (kW) and $\Delta t_{\mathscr{B}}$ is the accumulated duration of the evaluation interval (h). Energy and mean power were reported together to account for differ-

ences in seasonal duration.

The relative change in heating energy between the two cases was expressed as

$$\Delta E_{\text{wind}} = 100\ \frac{E_{\text{WIND}} - E_{\text{ZERO}}}{E_{\text{ZERO}}}, \tag{44}$$

where ΔE_{wind} is the percentage change and E_{WIND} and E_{ZERO} are heating energies over the same interval (kWh). Peak heating demand was defined as

$$P_{\text{peak}} = \max_{k} \left(\frac{Q_{\text{heat},k}}{1000} \right), \tag{45}$$

where P_{peak} is the maximum recorded interval heating power (kW). The critical sol was identified separately as the complete sol with the highest WIND heating energy. Consequently, peak interval power and maximum sol-integrated energy were treated as distinct performance measures.

Heating-demand exceedances were evaluated in terms of frequency, persistence, and severity, following the assessment approach used in an earlier study of Martian habitats by Görmez [22]. The indicators were adapted here to compare WIND and ZERO WIND using a common threshold.

The threshold was defined as

$$E_{\text{crit}} = \text{median}\,(\mathscr{E}) + \alpha\ \sigma_{\mathscr{E}}, \tag{46}$$

where $\mathscr{E}$ is the pooled set of complete-sol heating energies from both cases, E_{crit} is the threshold energy per sol (kWh), $\sigma_{\mathscr{E}}$ is the population standard deviation of the pooled values (kWh), and α is a dimensionless scaling parameter. The population standard deviation was calculated as

$$\sigma_{\mathscr{E}} = \sqrt{\frac{1}{M}\sum_{j=1}^{M} \left(E_j - \bar{E}_{\text{pool}} \right)^2}, \tag{47}$$

where $M = 1336$ is the number of pooled observations and $\bar{E}_{\text{pool}}$ is their arithmetic mean (kWh). The baseline threshold used $\alpha = 0.50$; sensitivity was evaluated at $\alpha = 0.40$, 0.60, and 0.70. For each value of α, the same threshold was applied to both cases. Pooling the two scenarios provides a common statistical reference, while varying α assesses whether the comparison depends on the selected threshold. The pooled median and population standard deviation were 507.853352 and 34.621470 kWh/sol, respectively, giving a baseline threshold of 525.164087 kWh/sol, reported as 525.16 kWh/sol. The baseline value α = 0.50 is an analysis choice for comparative screening, not an equipment-sizing or safety criterion.

A binary exceedance indicator was defined for each sol:

$$I_d = \begin{cases} 1, & E_d > E_{\text{crit}}, \\ 0, & E_d \le E_{\text{crit}}, \end{cases} \tag{48}$$

where E_d is the heating energy of sol d (kWh). The exceedance fraction was calculated as

$$FF = \frac{1}{N_S} \sum_{d=1}^{N_S} I_d , \tag{49}$$

where N_s = 668 is the number of complete sols and FF is dimensionless.

The longest consecutive exceedance duration was calculated as

$$LFS = \max_{\mathscr{R}} |\mathscr{R}| , \tag{50}$$

where $\mathscr{R}$ denotes a consecutive sequence of sols satisfying I_d = 1, and $|\mathscr{R}|$ is its length in sols. LFS was set to zero when no exceedance occurred.

The normalized exceedance-severity index was

$$FSI = \frac{1}{N_S} \sum_{d=1}^{N_S} \max \left(\frac{E_d - E_{\text{crit}}}{E_{\text{crit}}}, 0 \right) . \tag{51}$$

Here, FSI is dimensionless and represents the mean normalized exceedance over all complete sols, including those without exceedance. Together, FF, LFS, and FSI describe the frequency, persistence, and magnitude of elevated heating demand. The threshold serves as a comparative screening criterion rather than a prescribed heater-capacity limit or habitat safety requirement. Accordingly, these indicators alone do not demonstrate unmet heating demand, equipment failure, or operational risk.

Associations between WIND heating power and environmental variables were assessed using Spearman rank correlation [46]:

$$r_S = \text{corr} \left[R(x), R\left(Q_{\text{heat}}\right) \right] , \tag{52}$$

where $R(\cdot)$ denotes ranks, with average ranks assigned to tied values, and corr denotes Pearson correlation. The dimensionless coefficient r_s describes monotonic association. The evaluated variables were ambient temperature, ground temperature, global horizontal irradiance, direct normal irradiance, wind speed, and dust optical depth.

A season- and clock-adjusted rank correlation was also calculated as

$$r_{\text{adj}} = \text{corr} \left(e_x, e_Q \right) , \tag{53}$$

where e_x and e_Q are residuals obtained by separately regressing the ranked environmental variable and ranked heating power on a common harmonic basis. This basis comprised an intercept and the first two sine and cosine harmonics of solar longitude and model local solar time. The adjusted coefficient describes the remaining association after removing these fitted seasonal and diurnal components; it does not establish causality.

3. Results

3.1. Annual and Seasonal Heating Demand

Over the approximately one-Martian-year evaluation period, the total heating energy was 336.78 MWh for the WIND case and 328.78 MWh for the ZERO WIND case. Including wind increased heating demand by 7.99 MWh, corresponding to 2.43% relative to ZERO WIND. The mean heating powers over the same period were 20.43 kW and

19.94 kW, respectively.

Figure 2 presents the seasonal heating energy, mean heating power, and relative difference between the two cases over 30° solar-longitude intervals. Both cases exhibited a similar seasonal pattern, with higher heating requirements in WIND throughout all intervals. The lowest seasonal mean heating power occurred at L_s = 120°–150°, reaching 17.85 kW in WIND and 17.43 kW in ZERO WIND. The highest seasonal mean occurred at L_s = 270°–300°, with corresponding values of 22.27 kW and 21.79 kW. These values represent averages within the seasonal intervals rather than instantaneous peak loads.

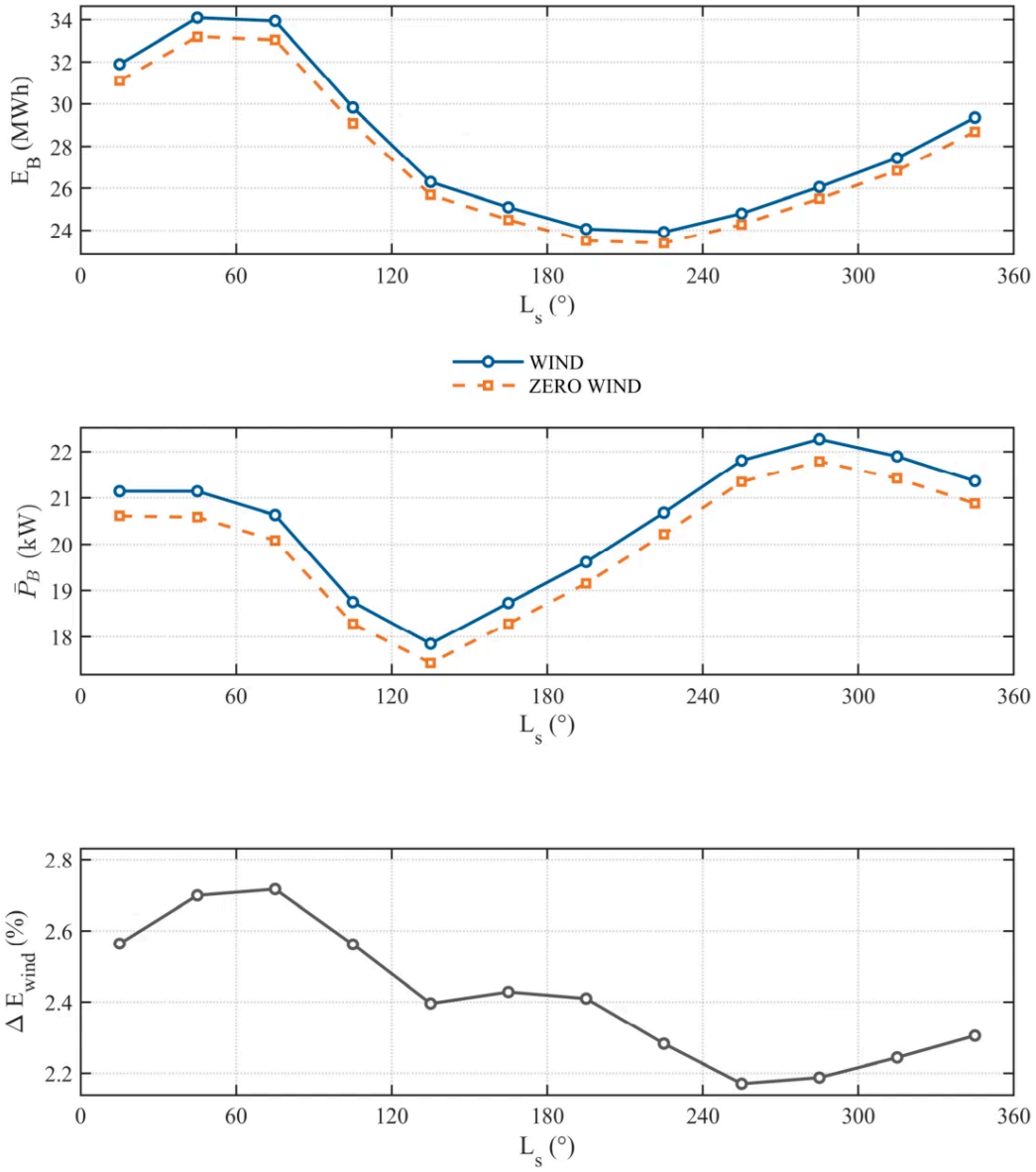

Figure 2. Seasonal comparison of WIND and ZERO WIND: (**a**) heating energy accumulated within 30° solar-longitude intervals; (**b**) mean heating power; and (**c**) percentage increase in heating energy relative to ZERO WIND.

The seasonal distribution of integrated heating energy differed from that of mean power because the solar-longitude intervals had unequal durations. The greatest heating energy occurred at L_s = 30°–60°, amounting to 34.10 MWh in WIND and 33.20 MWh in ZERO WIND, whereas the lowest occurred at L_s = 210°–240°, at 23.91 MWh and 23.38 MWh, respectively. Thus, the interval with the highest accumulated heating energy did not coincide with the interval having the highest mean heating power.

The relative increase associated with wind ranged from 2.17% to 2.72% across the seasonal intervals. The largest increase occurred at L_s = 60°–90°, while the smallest occurred at L_s = 240°–270°. Under the prescribed meteorological conditions and model assumptions, wind increased heating demand in every seasonal interval without changing the locations of the seasonal mean-power minimum and maximum.

3.2. Thermal Response During the Critical Sol

Sol 538 was identified as the critical sol because it exhibited the highest complete-sol heating energy in the WIND case. Heating energy reached 552.87 kWh in WIND and 541.10 kWh in ZERO WIND, corresponding to mean heating powers of 22.42 kW and 21.94 kW, respectively. Wind therefore increased heating energy by 11.77 kWh, or 2.18%, during this sol. The corresponding meteorological records covered approximately L_s = 284.36°–284.98°, within the seasonal interval associated with the highest mean heating power reported in Section 3.1.

Figure 3a shows similar within-sol heating profiles for the two cases. The maximum recorded 0.25 h step-average heating powers were 32.48 kW in WIND and 31.81 kW in ZERO WIND, occurring approximately 6.74 Earth hours after the sol began. The respective minima were 6.71 kW and 6.25 kW, both occurring at approximately 14.99 h. Heating remained necessary throughout the recorded period, although its magnitude varied substantially within the sol.

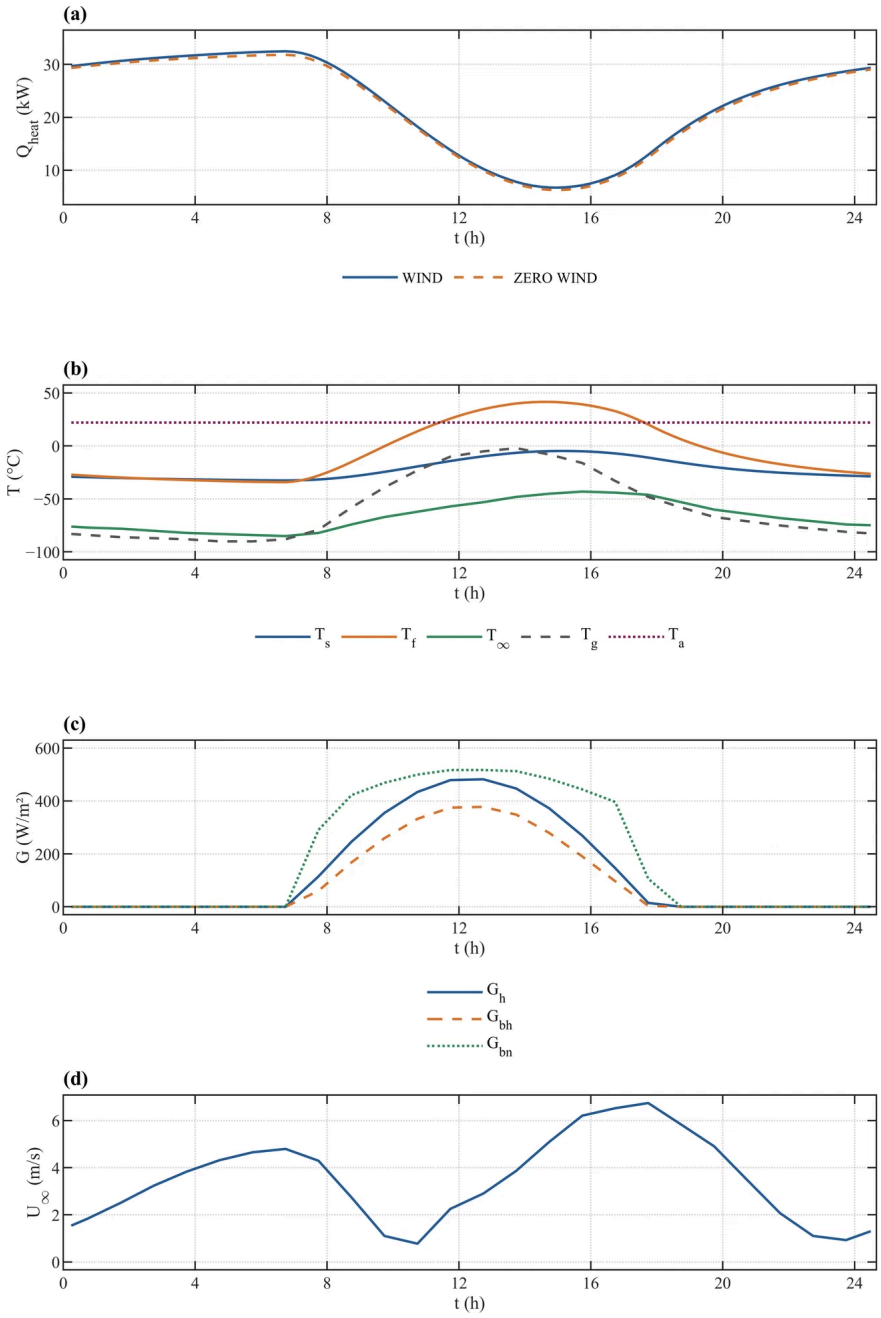

Figure 3. Thermal response and meteorological conditions during Sol 538: (**a**) heating power for WIND and ZERO WIND; (**b**) shell, floor, indoor-air, ambient-air, and ground temperatures for the WIND case; (**c**) global horizontal, direct horizontal, and direct normal irradiance; and (**d**) wind speed at the reference height. Time is expressed as elapsed Earth hours from the beginning of the sol.

In the WIND case, the indoor-air temperature remained at 22.00 °C to the reported precision, while the shell and floor temperatures exhibited pronounced variations (Figure 3b). Shell temperature ranged from −32.63 to −4.80 °C, whereas the floor/effective-

mass temperature ranged from −34.24 to 41.52 °C. Ambient-air and ground temperatures varied between −85.15 and −43.15 °C and between −90.15 and −2.15 °C, respectively. The recorded heating demand remained below the prescribed 100 kW heating-capacity limit.

Global horizontal irradiance reached 482.00 W/m^2, while direct horizontal and direct normal irradiance reached 377.64 W/m^2 and 517.20 W/m^2, respectively (Figure 3c). The maxima of global horizontal and direct normal irradiance occurred approximately 12.74 h after the sol began, preceding the minimum heating demand by 2.25 h. Wind speed at the reference height ranged from 0.78 to 6.74 m/s, reaching its maximum at approximately 17.74 h (Figure 3d). Thus, the maximum wind speed and maximum heating demand occurred at different times. The maximum recorded heating power coincided with the within-sol minimum ambient temperature and zero solar irradiance. Both scenarios nevertheless reached their maximum daily heating energy on Sol 538, indicating that the imposed wind contribution was not necessary for this sol to remain the critical day within the model. Wind increased its daily heating demand by 2.18%. The timing of the heating minimum after the irradiance maximum is consistent with the transient thermal response. Together, these observations support an interpretation involving cold conditions, the diurnal availability of solar gains, and thermal storage, with wind adding to the demand. They do not quantify the separate contributions of these factors to the annual maximum in daily heating energy.

Halving the time step increased daily heating energy on Sol 538 by 0.0017% for WIND and 0.0019% for ZERO WIND. These differences indicate low time-resolution sensitivity for the examined sol. Annual energy and threshold-exceedance sensitivity were not assessed by this short test, which does not constitute physical validation.

3.3. Associations Between Heating Demand and Environmental Variables

Figure 4 compares the overall Spearman correlations with the season- and clock-adjusted rank correlations between WIND heating power and six environmental variables. Ambient-air temperature exhibited the strongest negative overall association with heating demand (r_s = −0.980), followed by ground temperature (r_s = −0.946). After adjustment for the seasonal and diurnal harmonic components described in Section 2.7, both associations remained negative, with coefficients of r_{adj} = −0.806 and −0.781, respectively. Among the variables examined, these temperatures therefore retained the largest absolute correlation coefficients after adjustment.

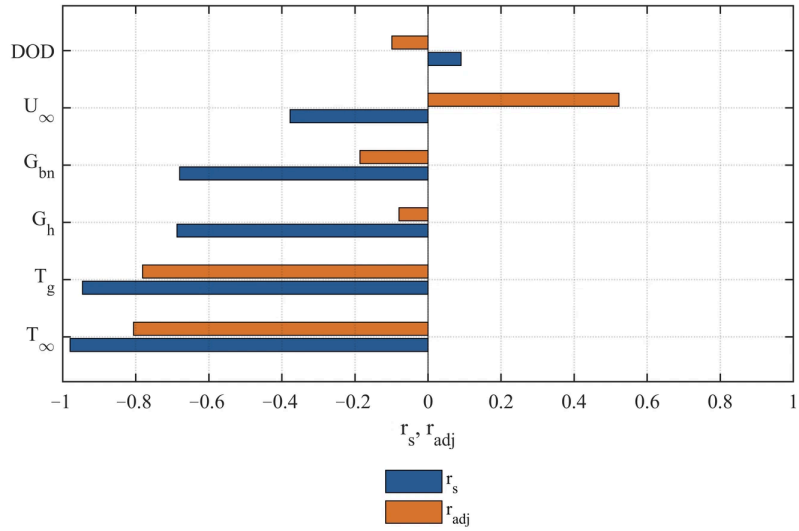

Figure 4. Overall Spearman and season- and clock-adjusted rank correlations between WIND heating power and ambient-air temperature, ground temperature, global horizontal irradiance, direct normal irradiance, wind speed, and dust optical depth. Adjusted coefficients were calculated after removing the fitted first- and second-order harmonics of solar longitude and model local solar time from the ranked series.

Global horizontal irradiance and direct normal irradiance also showed negative overall correlations with heating power, with r_s = −0.687 and −0.680, respectively. Their adjusted coefficients were substantially smaller in magnitude: r_{adj} = −0.079 for global horizontal irradiance and −0.186 for direct normal irradiance. Thus, much of their overall rank association with heating demand was attenuated after removing the fitted seasonal and diurnal components. These smaller adjusted coefficients do not imply that solar gains were thermally negligible.

Wind speed exhibited a change in correlation sign, from an overall coefficient of r_s = −0.377 to an adjusted coefficient of r_{adj} = 0.522. After the harmonic adjustment, higher wind-speed ranks were associated with higher heating-power ranks. This positive adjusted association is consistent in direction with the higher heating energy obtained in the WIND–ZERO WIND comparison, although the correlation analysis does not independently establish a causal effect.

Dust optical depth showed small correlation coefficients in both analyses, with r_s = 0.090 and r_{adj} = −0.099. These results describe associations within the prescribed simulation dataset. The adjustment removes the fitted solar-longitude and model-clock components; it does not isolate the independent effect of each environmental variable or control for all remaining covariation.

3.4. Integrated Solar and Heating Energy

Figure 5 compares the integrated solar energy absorbed by the shell, E_{abs}, the solar energy transmitted through the shell, E_{trans}, and the supplied heating energy, E_{heat}, for the WIND and ZERO WIND scenarios. Over the analysed period, absorbed and transmitted solar energy amounted to 23.11 and 207.96 MWh, respectively, in both scenarios. Transmitted solar energy was nine times the absorbed component, consistent with the prescribed shortwave transmittance and absorptance of 0.90 and 0.10.

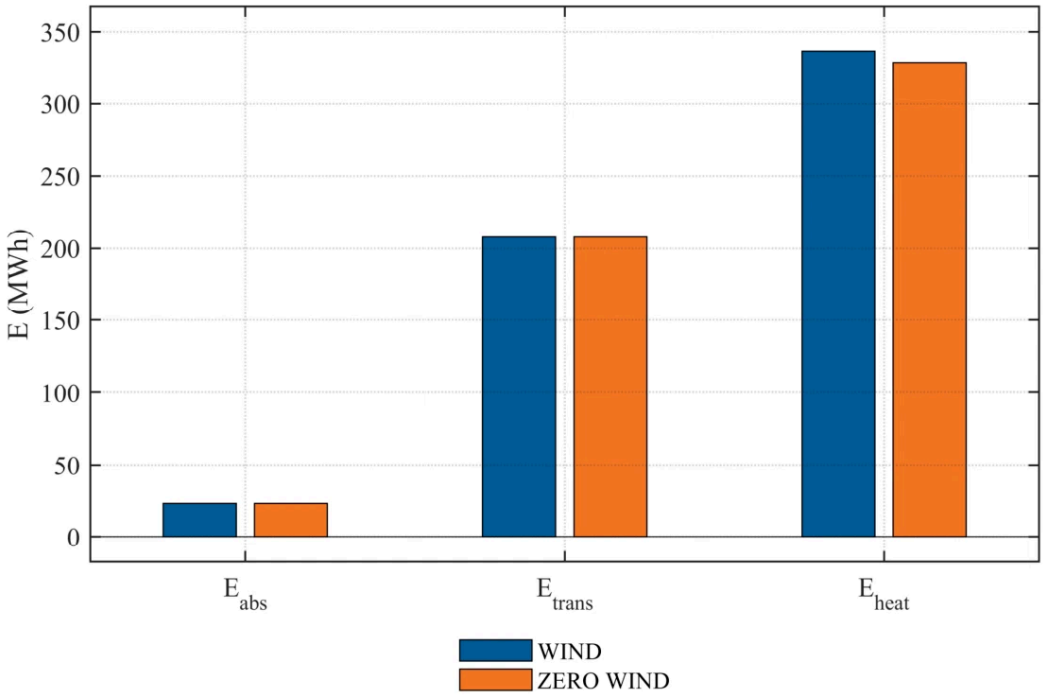

Figure 5. Integrated solar energy absorbed by the shell (E_{abs}), solar energy transmitted through the shell (E_{trans}), and supplied heating energy (E_{heat}) for the WIND and ZERO WIND scenarios.

Among the three reported components, heating energy was the largest in both scenarios. The identical solar energy totals indicate that the difference in heating demand occurred without a change in the integrated absorbed or transmitted solar input.

These quantities describe selected energy contributions rather than a complete energy balance. Convective and longwave radiative exchanges, ground heat transfer, and changes in stored thermal energy are not separately presented in Figure 5. Consequently, the transmitted solar energy cannot be interpreted directly as an equivalent reduction in heating demand.

3.5. Daily Heating Demand and Threshold-Exceedance Indicators

Figure 6 presents the variation in daily heating energy and mean heating power for the WIND and ZERO WIND scenarios. Daily heating energy ranged from 431.55 to 552.87 kWh in the WIND scenario and from 421.37 to 541.10 kWh in the ZERO WIND scenario. The minimum occurred on Sol 289 for WIND and Sol 290 for ZERO WIND, whereas both scenarios reached their maximum on Sol 538. WIND exhibited higher daily heating demand than ZERO WIND throughout the evaluated complete sols.

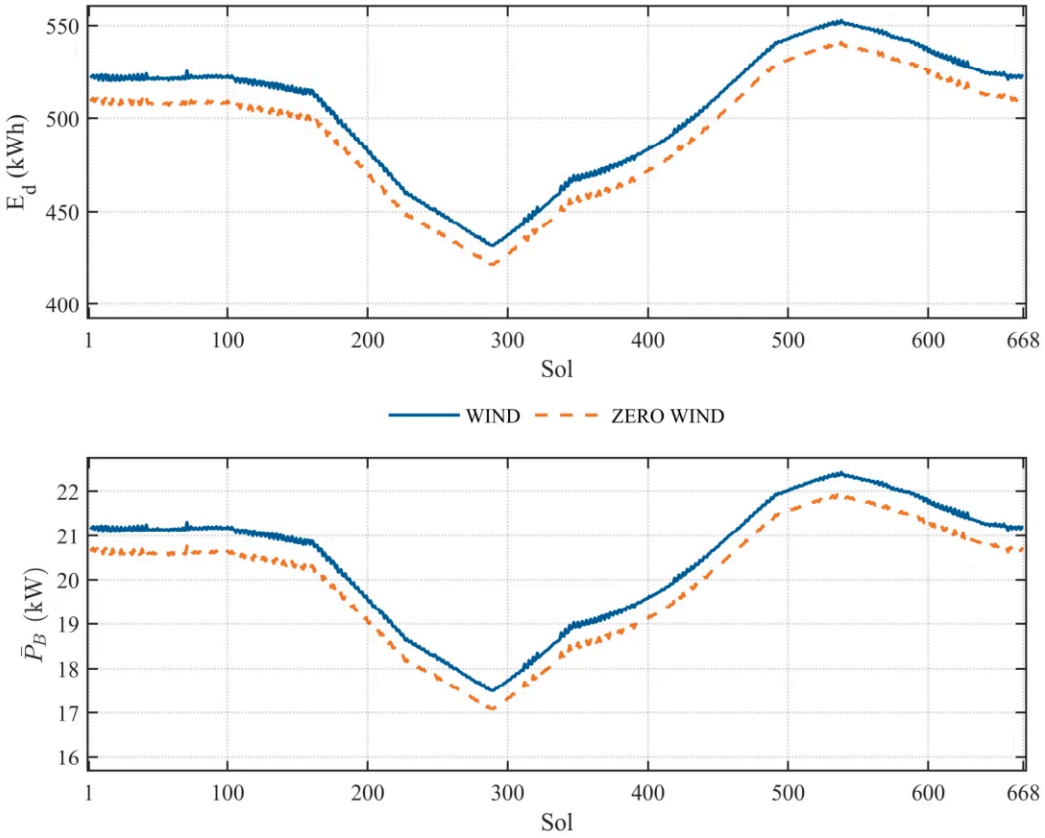

Figure 6. Daily heating energy and mean heating power for the WIND and ZERO WIND scenarios. Sol 1 is omitted from the displayed curves but retained in the indicator calculations.

For the baseline threshold parameter of $\alpha = 0.5$, the common daily energy threshold was 525.16 kWh/sol. This threshold was exceeded on 171 sols in the WIND scenario and 115 sols in the ZERO WIND scenario, corresponding to FF values of 0.2560 and 0.1722, respectively (Figure 7). The proportion of sols exceeding the threshold was therefore 8.38 percentage points higher under WIND. The longest continuous exceedance period, LFS, was 169 sols for WIND and 112 sols for ZERO WIND. These durations indicate that exceedances were predominantly concentrated in sustained periods rather than isolated events. The daily energy trajectories relative to the common threshold are presented in Figure 8.

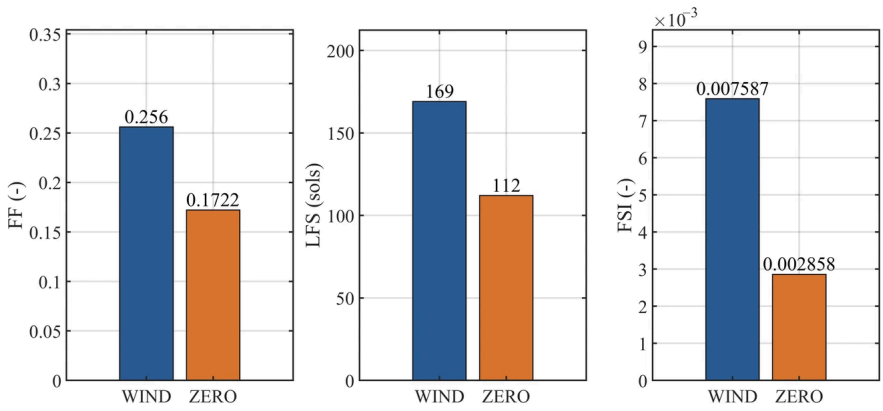

Figure 7. Comparison of FF, LFS, and FSI for the WIND and ZERO WIND scenarios at the baseline threshold of 525.16 kWh/sol ($\alpha = 0.5$).

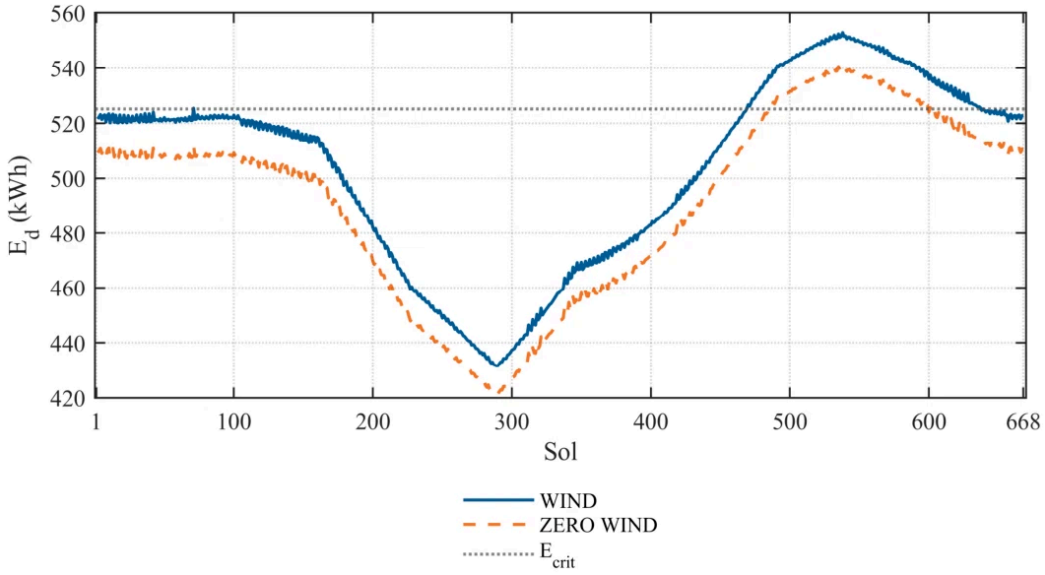

Figure 8. Daily heating energy for the WIND and ZERO WIND scenarios relative to the common threshold of 525.16 kWh/sol.

FSI was 0.00759 for WIND and 0.00286 for ZERO WIND (Figure 7). Because this indicator averages the positive normalized threshold excess over all evaluated sols, it reflects both the occurrence and magnitude of exceedances. Together, the three indicators show more frequent exceedances, a longer uninterrupted exceedance period, and a higher average normalized excess in the WIND scenario.

The threshold sensitivity analysis preserved this ordering across all tested values of α (Figure 9). Increasing α from 0.4 to 0.7 raised the threshold from 521.70 to 532.09 kWh/sol. Over this range, FF decreased from 0.3728 to 0.2051 for WIND and from 0.1961 to 0.1093 for ZERO WIND. LFS decreased from 193 to 135 sols and from 128 to 72 sols, respectively, while FSI decreased from 0.00962 to 0.00451 for WIND and from 0.00409 to 0.00092 for ZERO WIND. Although the indicator magnitudes depended on the selected threshold, WIND consistently produced higher values. These indicators characterize exceedances of the selected daily energy threshold; they do not establish heater failure or an inability to maintain the indoor temperature setpoint.

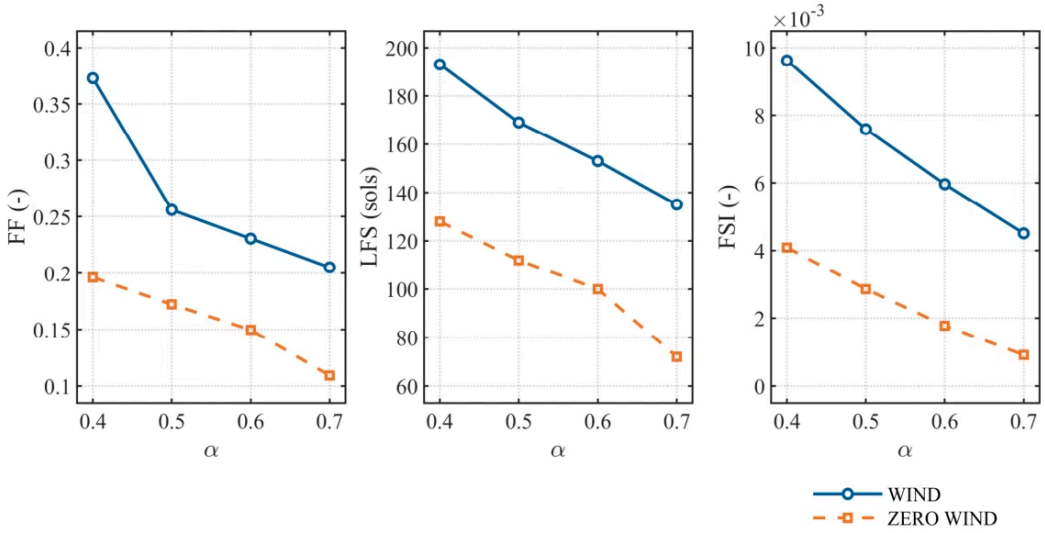

Figure 9. Sensitivity of FF, LFS, and FSI to the threshold parameter α for the WIND and ZERO WIND scenarios.

4. Discussion

Although annual heating demand increased by only 2.43% under WIND, the threshold analysis revealed more frequent and persistent periods of elevated daily demand. This distinction indicates that annual energy totals alone do not fully characterize the temporal distribution of heating requirements. Since the threshold is statistically defined rather than linked to equipment capacity, these indicators should not be interpreted as heating-system failure or operational risk.

Daily energy aggregation does not preserve within-sol power maxima. Figure 3 illustrates this distinction, but the reported power values represent 0.25 h step averages rather than instantaneous peaks. Shorter-duration heating requirements are therefore not resolved by these outputs. The short time-step comparison assessed daily energy sensitivity, not peak-power convergence. Consequently, the daily exceedance indicators cannot establish heater-capacity adequacy or exclude short-duration capacity exceedances.

For future system design, the demand profiles could be coupled to a specified energy-supply and storage model. A threshold linked to deliverable heating energy could then support screening of how frequently and persistently demand exceeds that reference. Assessing renewable or nuclear energy allocation would additionally require source-specific availability, conversion efficiency, and competing habitat loads, because the present outputs represent delivered heating energy rather than total electrical demand. Prolonged exceedance periods could help identify intervals for storage and reserve assessment, but resilience would need to be evaluated under explicitly defined supply interruptions or shortages. However, storage capacity would require a chronological supply–demand balance accounting for usable capacity, losses, charging opportunities, and power limits; LFS alone is not an autonomy requirement. Heater sizing would also require subdaily power demands, while generation reliability and reserve margins would require explicit availability and uncertainty assumptions. The present indicators identify periods warranting such assessments but do not determine equipment sizes or reliability levels.

Transmitted solar energy did not eliminate supplemental heating during the critical sol, emphasizing the need to consider solar gains alongside other heat-transfer processes. Martínez et al. [9] separately evaluated solar and infrared fluxes using MEDA observations at Jezero, providing an observational basis for assessing the local radiative environment. Those measurements offer a potential benchmark for the present boundary conditions, but do not constitute validation of the simulated habitat loads.

The reversal of the wind–heating correlation after temporal adjustment demonstrates the sensitivity of statistical associations to shared seasonal and diurnal variability.

The annual WIND simulation using the Yuge correlation reported by Will et al. [39], with thermophysical properties evaluated at the film temperature, yielded a heating demand of 336.523 MWh, compared with 336.778 MWh for the Whitaker reference. All other model settings and meteorological inputs were unchanged. The reduction of 0.255 MWh corresponds to 0.0756% of the reference total heating demand and approximately 3.19% of the original WIND–ZERO WIND energy difference. These results quantify sensitivity to the two implemented formulations, including their property-evaluation conventions, rather than providing independent validation of the sphere approximation for the geodesic dome.

In addition to wind-driven convection, surface-to-ambient temperature differences can induce buoyancy-driven flow, which may interact with the externally imposed flow [47]. Sun et al. [48] numerically investigated natural convection in horizontal and vertical CO_2 enclosures under Martian conditions and found orientation-dependent flow and

heat-transfer behaviour. These enclosure results cannot be directly transferred to external convection around the present dome. In the present model, setting wind speed to zero removes the wind-dependent terms while retaining the spherical conduction limit, Nu = 2; natural convection is not separately modelled. The WIND–ZERO WIND comparison therefore isolates the wind-dependent contribution within the adopted formulation. Explicitly including natural or mixed convection could affect the heating demands of both cases, but the magnitude of this annual effect cannot be inferred from the Whitaker–Yuge comparison.

The selected parameters influence heating demand through different terms of the coupled energy balances. Shell thickness, density and specific heat determine shell thermal capacity, while the prescribed floor capacity represents effective thermal storage. These capacities govern the transient temperature response. Solar absorptance and transmittance determine the solar gains assigned to the shell and floor, while longwave properties and heat-transfer coefficients govern radiative and thermal exchanges. The equivalent shell thickness and selected ETFE optical properties were adopted with reference to [20], while ETFE density, specific heat and solar transmittance were taken from [30]. Floor thermal capacity and internal heat-transfer coefficients were prescribed model inputs. In particular, the thin-film solar transmittance is not a measured property of the adopted 18 mm equivalent shell. Keeping these inputs unchanged between WIND and ZERO WIND provides a consistent comparison, but does not establish insensitivity to parameter uncertainty. Their individual effects on annual heating demand have not been quantified through a material-parameter sensitivity analysis. A short-duration, standalone Python sensitivity test was conducted for Sol 538 using the existing thermal-model functions, matched initial states, and otherwise unchanged settings. Reducing ETFE specific heat from 1172 to 900 J/(kg K) [49] increased daily heating energy by 0.0296% in WIND and 0.0338% in ZERO WIND. The maximum absolute shell-temperature differences relative to the reference at corresponding times were 1.44 K and 1.43 K, respectively. This test was not an annual TRNSYS–Python assessment and does not establish annual sensitivity or physically validate the equivalent envelope.

Meteorological forcing introduces additional uncertainty. Differences between atmospheric-model predictions for Jezero, particularly in near-surface winds [5], indicate that the prescribed climate series should not be treated as an exact environmental record. Temperature and radiative-input uncertainties affect the imposed thermal boundary conditions, while wind speed and MCD-derived atmospheric density enter the external convection calculation. Atmospheric pressure is not independently varied in the thermal model. Dust-related radiative uncertainty concerns the supplied MCD irradiance; dust optical depth is not applied as an additional attenuation factor in the Python thermal model. The present comparison therefore does not quantify sensitivity to alternative meteorological or dust scenarios. Together with the thermal-parameter assumptions discussed above, these uncertainties may influence both absolute heating demand and the WIND–ZERO WIND difference. Consistent assumptions between scenarios do not guarantee cancellation of uncertainty. These uncertainties were not quantitatively propagated through the model; therefore, the 2.43% difference has not been shown to exceed their combined influence. It should be interpreted as a conditional modelled difference under the prescribed inputs and assumptions. The annual Whitaker–Yuge comparison supports limited sensitivity to that particular modelling choice, but does not provide an overall uncertainty bound.

The available sensitivity assessments address convection-formulation choice, the statistical exceedance threshold, and short-window ETFE specific-heat sensitivity, rather than providing a comprehensive ranking of environmental and design parameters.

Future work should systematically evaluate their effects on annual heating energy, maximum daily demand, and exceedance frequency and duration. Such an assessment should use physically justified parameter ranges and account for dependencies between inputs. Envelope thermal resistance and non-heating internal gains would require explicit representation in an extended model.

The quantitative findings are specific to the selected Jezero climate scenario and habitat configuration. Within this case, WIND increased heating demand in every analysed seasonal interval, and higher exceedance indicators persisted across the tested thresholds. These comparisons do not establish generalizability to other locations, habitat dimensions, or envelope configurations. Changes in geometry, thermal storage, optical properties, and environmental forcing could alter both the relative wind contribution and the duration of threshold exceedances. The combined assessment of annual energy and demand persistence is transferable as an analytical approach, whereas the reported magnitudes and scenario ordering require reassessment for each new configuration.

The predictions remain conditional on the lumped thermal representation, prescribed material properties, and external convection model. Independent validation of dome-scale heat transfer remains necessary before using the predictions for thermal-control sizing.

Physics-informed neural networks have been applied to heat-transfer problems [50]. A possible future extension is a physics-informed neural network incorporating the three-node energy balances and initial conditions into its training objective. Its accuracy and computational cost would need to be assessed against the existing numerical solver, while physical validation would require independent reference data. This approach was not implemented in the present study.

5. Conclusions

The coupled model predicted annual heating demands of 336.78 MWh under WIND and 328.78 MWh under ZERO WIND, corresponding to a 2.43% increase. Despite this relatively modest annual difference, the WIND scenario exhibited more frequent and persistent exceedances of the common daily heating-energy threshold. The findings indicate the complementary value of annual energy assessment and temporal demand indicators.

The findings apply to the specified habitat and boundary conditions; the exceedance indicators characterize demand relative to a selected threshold rather than demonstrated heating-system failure. The results should be interpreted as preliminary model-based estimates, as the adopted thermal representation and external convection formulation have not been independently validated under Martian habitat conditions.

Author Contributions: Conceptualization, G.G. and D.M.; methodology, G.G. and D.M.; software, G.G. and D.M.; formal analysis, G.G. and D.M.; investigation, G.G. and D.M.; data curation, G.G. and D.M.; visualization, G.G. and D.M.; writing—original draft preparation, G.G. and D.M.; writing—review and editing, G.G. and D.M.; supervision, D.M. All authors have read and agreed to the published version of the manuscript.

Funding: This research received no external funding.

Institutional Review Board Statement: Not applicable. This study involved numerical simulations and did not involve human participants or animals.

Informed Consent Statement: Not applicable.

Data Availability Statement: The simulation input files, model and post-processing scripts, and numerical outputs supporting the reported findings are available from the corresponding author

upon reasonable request. The meteorological inputs were derived from the Mars Climate Database, version 6.1; access to the underlying database is subject to its providers' terms.

Acknowledgments: During the preparation of this study and manuscript, the authors used OpenAI ChatGPT and Codex GPT-6 Astra to assist with manuscript drafting and language editing, code review and revision, and the preparation and checking of data visualizations. The authors reviewed and edited the resulting text, code, and figures and take responsibility for the content of this publication.

Conflicts of Interest: The authors declare no conflicts of interest.

Nomenclature

The principal symbols used in this manuscript are listed below.

Symbol	Definition	Unit
A	Area	m^2
C	Thermal capacitance	J/K
c_p	Specific heat capacity	J/(kg·K)
D	Habitat diameter	m
E	Energy	kWh or MWh
F	Radiation view factor	-
G	Solar irradiance	W/m^2
H	Irradiation in the radiation model	W/m^2
h	Heat-transfer coefficient	$W/(m^2·K)$
J	Radiosity	W/m^2
k	Thermal conductivity	W/(m·K)
L_s	Solar longitude	°
Nu_D, Re_D, Pr	Nusselt, Reynolds, and Prandtl numbers	-
P	Heating power	kW
Q	Heat-transfer rate or heating power	W
r	Habitat radius	m
r_s, r_{adj}	Spearman and adjusted rank correlation coefficients	-
T	Temperature	K or °C
t	Time	s or h
U	Wind speed	m/s
V	Habitat volume	m^3
α	Threshold scaling parameter	-
α_{sol}	Solar absorptance	-
δ_{shell}	Shell thickness	m
ε_s, ε_f, ε_g	Longwave emissivities of the shell, floor, and ground	-
μ	Dynamic viscosity	kg/(m·s)
ρ	Density	kg/m^3
σ	Stefan–Boltzmann constant	$W/(m^2·K^4)$

σ_E	Population standard deviation of pooled heating energies	kWh
τ	Radiative transmittance	-

Abbreviations

The following abbreviations are used in this manuscript:

MCD	Mars Climate Database
MEDA	Mars Environmental Dynamics Analyzer
ETFE	Ethylene tetrafluoroethylene
TRNSYS	Transient System Simulation Program
FF	Exceedance fraction
LFS	Longest consecutive exceedance duration
FSI	Normalized exceedance-severity index
DOD	Dust optical depth

References

1. Guan, L.; Li, L.; Creecy, E.C.; Jiang, X.; Wang, X.; Martínez, G.; Toigo, A.D.; Richardson, M.I.; Sánchez-Lavega, A.; Lee, Y.J. Distinct Energy Budgets of Mars and Earth. *AGU Adv.* **2024**, *5*, e2024AV001389. [Google Scholar] [CrossRef]
2. Appelbaum, J.; Flood, D.J. *Solar Radiation on Mars*; NASA (National Aeronautics and Space Administration): Cleveland, OH, USA, 1989.
3. Li, J.; Bai, Y.; Bi, S.; Beer, M. Thermomechanical Behavior of Steel Structural Configurations Subjected to Cyclic Cryogenic Conditions in Martian Environment. *Adv. Space Res.* **2025**, *76*, 3700–3716. [Google Scholar] [CrossRef]
4. Forget, F.; Hourdin, F.; Fournier, R.; Hourdin, C.; Talagrand, O.; Collins, M.; Lewis, S.R.; Read, P.L.; Huot, J.P. Improved General Circulation Models of the Martian Atmosphere from the Surface to above 80 km. *J. Geophys. Res. Planets* **1999**, *104*, 24155–24175. [Google Scholar] [CrossRef]
5. Newman, C.E.; de la Torre Juárez, M.; Pla-García, J.; Wilson, R.J.; Lewis, S.R.; Neary, L.; Kahre, M.A.; Forget, F.; Spiga, A.; Richardson, M.I.; et al. Multi-Model Meteorological and Aeolian Predictions for Mars 2020 and the Jezero Crater Region. *Space Sci. Rev.* **2021**, *217*, 20. [Google Scholar] [CrossRef] [PubMed]
6. Rodriguez-Manfredi, J.A.; de la Torre Juárez, M.; Alonso, A.; Apéstigue, V.; Arruego, I.; Atienza, T.; Banfield, D.; Boland, J.; Carrera, M.A.; Castañer, L.; et al. The Mars Environmental Dynamics Analyzer, MEDA. A Suite of Environmental Sensors for the Mars 2020 Mission. *Space Sci. Rev.* **2021**, *217*, 48. [Google Scholar] [CrossRef] [PubMed]
7. Rodriguez-Manfredi, J.A.; de la Torre Juarez, M.; Sanchez-Lavega, A.; Hueso, R.; Martinez, G.; Lemmon, M.T.; Newman, C.E.; Munguira, A.; Hieta, M.; Tamppari, L.K.; et al. The Diverse Meteorology of Jezero Crater over the First 250 Sols of Perseverance on Mars. *Nat. Geosci.* **2023**, *16*, 19–28. [Google Scholar] [CrossRef]
8. Munguira, A.; Hueso, R.; Sánchez-Lavega, A.; de la Torre-Juarez, M.; Martínez, G.M.; Newman, C.E.; Sebastian, E.; Lepinette, A.; Vicente-Retortillo, A.; Chide, B.; et al. Near Surface Atmospheric Temperatures at Jezero From Mars 2020 MEDA Measurements. *J. Geophys. Res. Planets* **2023**, *128*, e2022JE007559. [Google Scholar] [CrossRef]
9. Martínez, G.M.; Sebastián, E.; Vicente-Retortillo, A.; Smith, M.D.; Johnson, J.R.; Fischer, E.; Savijärvi, H.; Toledo, D.; Hueso, R.; Mora-Sotomayor, L.; et al. Surface Energy Budget, Albedo, and Thermal Inertia at Jezero Crater, Mars, as Observed From the Mars 2020 MEDA Instrument. *J. Geophys. Res. Planets* **2023**, *128*, e2022JE007537. [Google Scholar] [CrossRef]
10. Smith, M.D.; Martínez, G.M.; Sebastián, E.; Lemmon, M.T.; Wolff, M.J.; Apéstigue, V.; Arruego, I.; Toledo, D.; Viúdez-Moreiras, D.; Rodriguez-Manfredi, J.A.; et al. Diurnal and Seasonal Variations of Aerosol Optical Depth Observed by MEDA/TIRS at Jezero Crater, Mars. *J. Geophys. Res. Planets* **2023**, *128*, e2022JE007560. [Google Scholar] [CrossRef]
11. Viúdez-Moreiras, D.; Lemmon, M.; Newman, C.E.; Guzewich, S.; Mischna, M.; Gómez-Elvira, J.; Herkenhoff, K.; Sánchez-Lavega, A.; de la Torre, M.; Rodríguez-Manfredi, J.A.; et al. Winds at the Mars 2020 Landing Site: 1. Near-Surface Wind Patterns at Jezero Crater. *J. Geophys. Res. Planets* **2022**, *127*, e2022JE007522. [Google Scholar] [CrossRef]

12. de la Torre Juárez, M.; Chavez, A.; Tamppari, L.K.; Munguira, A.; Martínez, G.; Hueso, R.; Chide, B.; Murdoch, N.; Stott, A.E.; Navarro, S.; et al. Diurnal Cycle of Rapid Air Temperature Fluctuations at Jezero Crater: Probability Distributions, Exponential Tails, Scaling, and Intermittency. *J. Geophys. Res. Planets* **2023**, *128*, e2022JE007458. [Google Scholar] [CrossRef]
13. Sánchez-Lavega, A.; del Rio-Gaztelurrutia, T.; Hueso, R.; de la Torre Juárez, M.; Martínez, G.M.; Harri, A.M.; Genzer, M.; Hieta, M.; Polkko, J.; Rodríguez-Manfredi, J.A.; et al. Mars 2020 Perseverance Rover Studies of the Martian Atmosphere over Jezero from Pressure Measurements. *J. Geophys. Res. Planets* **2023**, *128*, e2022JE007480. [Google Scholar] [CrossRef] [PubMed]
14. Hueso, R.; Newman, C.E.; del Río-Gaztelurrutia, T.; Munguira, A.; Sánchez-Lavega, A.; Toledo, D.; Apéstigue, V.; Arruego, I.; Vicente-Retortillo, A.; Martínez, G.; et al. Convective Vortices and Dust Devils Detected and Characterized by Mars 2020. *J. Geophys. Res. Planets* **2023**, *128*, e2022JE007516. [Google Scholar] [CrossRef]
15. Toledo, D.; Apéstigue, V.; Arruego, I.; Lemmon, M.; Gómez, L.; Montoro, F.; Hueso, R.; Newman, C.; Smith, M.; Viudez-Moreiras, D.; et al. Dust Devil Frequency of Occurrence and Radiative Effects at Jezero Crater, Mars, as Measured by MEDA Radiation and Dust Sensor (RDS). *J. Geophys. Res. Planets* **2023**, *128*, e2022JE007494. [Google Scholar] [CrossRef]
16. Vicente-Retortillo, A.; Martínez, G.M.; Lemmon, M.T.; Hueso, R.; Johnson, J.R.; Sullivan, R.; Newman, C.E.; Sebastián, E.; Toledo, D.; Apéstigue, V.; et al. Dust Lifting Through Surface Albedo Changes at Jezero Crater, Mars. *J. Geophys. Res. Planets* **2023**, *128*, e2022JE007672. [Google Scholar] [CrossRef]
17. Vicente-Retortillo, A.; Lemmon, M.T.; Martinez, G.M.; Toledo, D.; Apéstigue, V.; Arruego, I.; Bertrand, T.; Lorenz, R.; Sebastián, E.; Hueso, R.; et al. Dust Accumulation and Lifting at the Landing Site of the Mars 2020 Mission, Jezero Crater, as Observed From MEDA. *Geophys. Res. Lett.* **2024**, *51*, e2023GL107975. [Google Scholar] [CrossRef]
18. Lemmon, M.T.; Smith, M.D.; Viudez-Moreiras, D.; de la Torre-Juarez, M.; Vicente-Retortillo, A.; Munguira, A.; Sanchez-Lavega, A.; Hueso, R.; Martinez, G.; Chide, B.; et al. Dust, Sand, and Winds Within an Active Martian Storm in Jezero Crater. *Geophys. Res. Lett.* **2022**, *49*, e2022GL100126. [Google Scholar] [CrossRef] [PubMed]
19. Jadeja, A.; Jaiswal, M.M.; Ghosh, S.; Sanghavi, P. Thermal Comfort Analysis of a Proposed Design for a Sustainable Living Space on Mars. *Intell. Build. Int.* **2016**, *8*, 215–233. [Google Scholar] [CrossRef]
20. Salgado-Rodriguez, M.; Garcia-Luis, U.; Gomez-San-Juan, A.; Ulloa-Sande, C.; Navarro-Medina, F. Conceptual Design and Research on the Thermal Performance of a Martian Human Base. *Acta Astronaut.* **2022**, *200*, 524–538. [Google Scholar] [CrossRef]
21. Kömle, N.I.; Herzig, T.; Macher, W.; Gläser, P.; Bihari, G. Site Selection and Thermal Model for a Mars Habitat Built from Inflatable Components in the Valles Marineris Region. *Planet. Space Sci.* **2025**, *269*, 106216. [Google Scholar] [CrossRef]
22. Görmez, G. Failure-Oriented Thermal Performance Assessment of Martian Habitats: A Risk-Based Framework. *Acta Astronaut.* **2027**, *250*, 462–474. [Google Scholar] [CrossRef]
23. Charoenboonvivat, Y.; de Weck, O. Surface Power Demand Modeling for Human Martian and Lunar Missions. In Proceedings of the AIAA SCITECH 2026 Forum, American Institute of Aeronautics and Astronautics, Orlando, FL, USA, 12–16 January 2026. [Google Scholar]
24. Porta-Gándara, M.A.; Gómez-Muñoz, V. Solar Performance of an Electrochromic Geodesic Dome Roof. *Energy* **2005**, *30*, 2474–2486. [Google Scholar] [CrossRef]
25. Assoa, Y.B.; Levrard, D. A Lightweight Triangular Building Integrated Photovoltaic Module. *Appl. Energy* **2020**, *279*, 115816. [Google Scholar] [CrossRef]
26. Millour, E.; Forget, F.; Spiga, A.; Pierron, T.; Bierjon, A.; Montabone, L.; Vals, M.; Lefèvre, F.; Chaufray, J.-Y.; Lopez-Valverde, M.; et al. The Mars Climate Database (Version 6.1). In Proceedings of the Europlanet Science Congress 2022, Granada, Spain, 18–23 September 2022; Volume 16, p. EPSC2022-786. [Google Scholar]
27. Millour, E.; Forget, F.; Pierron, T.; Lewis, S.R.; MCD Team. *Mars Climate Database v6.1 User Manual*; Laboratoire de Météorologie Dynamique (LMD): Paris, France, 2022. [Google Scholar]
28. Forget, F.; Millour, E.; Pierron, T.; Vals, M.; Zakharov, V.; MCD team. *Mars Climate Database v6.1: Detailed Design Document*; Laboratoire de Météorologie Dynamique (LMD): Paris, France, 2022. [Google Scholar]
29. Allison, M.; McEwen, M. A Post-Pathfinder Evaluation of Areocentric Solar Coordinates with Improved Timing Recipes for Mars Seasonal/Diurnal Climate Studies. *Planet. Space Sci.* **2000**, *48*, 215–235. [Google Scholar] [CrossRef]
30. The Chemours Company. *Tefzel ETFE Fluoropolymer Film: Properties Bulletin*; DuPont de Nemours, Inc.: Wilmington, DE, USA, 2025. [Google Scholar]
31. Allison, M.; Schmunk, R. *Technical Notes on Mars Solar Time as Adopted by the Mars24 Sunclock 2023*; NASA Goddard Institute for Space Studies: New York, NY, USA, 2023.

32. Pvlib Python Contributors. *Pvlib.Irradiance.Beam_component*, pvlib-python. Available online: https://pvlib-python.readthedocs.io/en/stable/reference/generated/pvlib.irradiance.beam_component.html (accessed on 19 November 2026).
33. Sandia National Laboratories. *Isotropic Sky Diffuse Model*; Sandia National Laboratories: Livermore, CA, USA. Available online: https://pvpmc.sandia.gov/modeling-guide/1-weather-design-inputs/plane-of-array-poa-irradiance/calculating-poa-irradiance/poa-sky-diffuse/isotropic-sky-diffuse-model/?utm_source=chatgpt.com (accessed on 19 November 2026).
34. Frei, W. *Introduction to Computing Radiative Heat Exchange* COMSOL, Inc.: Burlington, MA, USA, 2022. Available online: https://www.comsol.com/blogs/introduction-to-computing-radiative-heat-exchange (accessed on 19 November 2026).
35. Frei, W. *Modeling Incident Radiation in Radiative Heat Transfer* COMSOL, Inc.: Burlington, MA, USA, 2022. Available online: https://www.comsol.com/blogs/modeling-incident-radiation-in-radiative-heat-transfer (accessed on 19 November 2026).
36. Whitaker, S. Forced Convection Heat Transfer Correlations for Flow in Pipes, Past Flat Plates, Single Cylinders, Single Spheres, and for Flow in Packed Beds and Tube Bundles. *AIChE J.* **1972**, *18*, 361–371. [Google Scholar] [CrossRef]
37. Soria-Salinas, Á.; Zorzano, M.-P.; Mantas-Nakhai, R.; Martín-Torres, J. Development of a Wind Retrieval Method for Low-Speed Low-Pressure Flows for ExoMars. *Appl. Therm. Eng.* **2020**, *180*, 115752. [Google Scholar] [CrossRef]
38. Domínguez-Pumar, M.; Kowalski, L.; Jiménez, V.; Rodríguez, I.; Soria, M.; Bermejo, S.; Pons-Nin, J. Analyzing the Performance of a Miniature 3D Wind Sensor for Mars. *Sensors* **2020**, *20*, 5912. [Google Scholar] [CrossRef] [PubMed]
39. Will, J.B.; Kruyt, N.P.; Venner, C.H. An Experimental Study of Forced Convective Heat Transfer from Smooth, Solid Spheres. *Int. J. Heat Mass Transf.* **2017**, *109*, 1059–1067. [Google Scholar] [CrossRef]
40. COMSOL. Sutherland's Law. COMSOL Multiphysics Documentation, Version 6.4. Available online: https://doc.comsol.com/6.4/doc/com.comsol.help.cfd/cfd_ug_fluidflow_high_mach.08.46.html (accessed on 17 November 2026).
41. Yamashita, T.; Odaka, M.; Sugiyama, K.I.; Nakajima, K.; Ishiwatari, M.; Nishizawa, S.; Takahashi, Y.O.; Hayashi, Y.Y. A Numerical Study of Convection in a Condensing CO2 Atmosphere under Early Mars-like Conditions. *J. Atmos. Sci.* **2016**, *73*, 4151–4169. [Google Scholar] [CrossRef]
42. Osczevski, R. Martian Windchill in Terrestrial Terms. *Bull. Am. Meteorol. Soc.* **2014**, *95*, 533–541. [Google Scholar] [CrossRef]
43. Thermal Energy System Specialists. *TRNSYS 18: A Transient System Simulation Program*; Thermal Energy System Specialists, LLC: Madison, WI, USA, 2017. [Google Scholar]
44. Moler, C. Chapter 7: Ordinary Differential Equations. In *Numerical Computing with MATLAB*; Society for Industrial and Applied Mathematics: Philadelphia, PA, USA, 2013. [Google Scholar]
45. GNU Scientific Library One-Dimensional Root-Finding. Available online: https://www.gnu.org/software/gsl/doc/html/roots.html (accessed on 19 November 2026).
46. SciPy contributors.*scipy.stats.spearmanr*. SciPy Documentation. Available online: https://docs.scipy.org/doc/scipy/reference/generated/scipy.stats.spearmanr.html (accessed on 19 November 2026).
47. Yovanovich, M.M.; Vanoverbeke, C.A. Combined Natural and Forced Convection Heat Transfer from Isothermal Spheres. In *Proceedings of the AIAA Thermophysics, Plasmadynamics and Lasers Conference*; American Institute of Aeronautics and Astronautics: San Antonio, TX, USA, 1988; pp. 1–7. [Google Scholar]
48. Sun, Y.; Lin, G.; Bu, X.; Bai, L.; Xiao, C.; Wen, D. A Numerical Study of Fluid Flow and Heat Transfer in Carbon Dioxide Enclosures on Mars. *Energies* **2018**, *11*, 756. [Google Scholar] [CrossRef]
49. NETZSCH Analyzing & Testing. ETFE: Ethylene-Tetrafluoroethylene. Available online: https://analyzing-testing.netzsch.com/en-US/polymers-netzsch-com/high-temperature-resistant-thermoplastics/etfe-ethylene-tetrafluoroethylene (accessed on 17 November 2026).
50. Cai, S.; Wang, Z.; Wang, S.; Perdikaris, P.; Karniadakis, G.E. Physics-Informed Neural Networks for Heat Transfer Problems. *J. Heat Transfer* **2021**, *143*, 60801. [Google Scholar] [CrossRef]

Disclaimer/Publisher's Note: The statements, opinions and data contained in all publications are solely those of the individual author(s) and contributor(s) and not of MDPI and/or the editor(s). MDPI and/or the editor(s) disclaim responsibility for any injury to people or property resulting from any ideas, methods, instructions or products referred to in the content.